Can the mechanoreceptional setae of a feeding-current feeding copepod detect hydrodynamic disturbance induced by entrained free-floating prey?

Shen, Xinhui; Yao, Xin; Marcos; Fu, Henry C.

2021

Shen, X., Yao, X., Marcos & Fu, H. C. (2021). Can the mechanoreceptional setae of a feeding-current feeding copepod detect hydrodynamic disturbance induced by entrained free-floating prey?. Limnology and Oceanography, 66(12), 4096-4111. https://dx.doi.org/10.1002/lno.11945

https://hdl.handle.net/10356/153648

https://doi.org/10.1002/lno.11945

Can the mechanoreceptional setae of a feeding-current feeding copepod detect hydrodynamic disturbance induced by entrained free-floating prey?

Xinhui Shen[1], Xin Yao[1], Marcos[1*], Henry C. Fu[2*]

[1] School of Mechanical and Aerospace Engineering, Nanyang Technological University, Singapore

[2] Department of Mechanical Engineering, University of Utah, Salt Lake City, Utah 84112, USA

ORCID ID for Marcos: https://orcid.org/0000-0001-5657-196X

ORCID ID for Henry C. Fu: https://orcid.org/0000-0002-3543-7128

Email address for authors (listed in sequence): xshen006@e.ntu.edu.sg, yaoxin@ntu.edu.sg, marcos@ntu.edu.sg, henry.fu@utah.edu

* Correspondence: marcos@ntu.edu.sg, henry.fu@utah.edu

Running head: Prey detection in feeding currents

Key Words: copepods, seta, mechanoreception, feeding-current feeding, prey detection, hydrodynamic sensitivity, setal deformation

Abstract

Copepods that catch prey using feeding currents beat their cephalic appendages to generate flow entrainment, and detect the presence of nearby prey through the mechanoreceptional setae on the antennules and other appendages. It remains unclear whether the feeding current can be used by the copepod to gain information about its surroundings by sensing when the current is disturbed by nearby particles. In this article, we present a numerical model to address how much the presence of free-floating prey can alter the feeding current velocity field, and how these prey-induced disturbances modify setal deformation patterns. We prescribe the beating strokes of the feeding appendages, and quantify the changes in the bending flows across the setae and setal deformations due to the prey entrainment. We find that, first, the seta bends more due to the time-averaged velocity component of the feeding current, while filtering out the oscillatory component. Second, 100 μm diameter free-floating prey do not induce any noticeable change in deformations of the proximal and distal setae unless they are less than 10 or 5.5 prey radii from the antennules, respectively. Larger prey cause bigger flow disturbances than small prey, which are expected to be even harder to detect. Last, if setae are responsive to changes in deformation *relative* to the deformations in the absence of prey, the distal seta may have long-ranged sensitivity to assist in detection of prey near the proximal seta, but if setae are responsive to *absolute* changes in deformation, both setae have very short-ranged sensitivity.

Introduction

Feeding-current and cruise feeding copepods achieve prey detection by beating their cephalic appendages, pulling both motile and free-floating planktonic prey towards their mouthpart (Koehl and Strickler 1981; Strickler 1982), and sensing their presence through the mechanoreceptional and/or chemoreceptional setae protruding from the antennules and other

appendages (Paffenhöfer and Loyd 1999; Strickler and Bal 1973; Yen et al. 1992). Mechanoreception is postulated to be more efficient than chemoreception for feeding-current feeding copepods (Gonçalves and Kiørboe 2015). The mechanoreception of copepods starts when the prey-induced signal -- either hydrodynamic disturbance or direct contact (Kiørboe et al. 2014; Kjellerup and Kiørboe 2012; Paffenhöfer and Van Sant 1985) -- bends the thin long mechanoreceptional seta to a certain extent (Fields et al. 2002). Setal deformation is then transformed into neurophysiological signals through mechanotransduction, in which opening of mechano-gated microchannels perforating the membrane of the dendrite attached to the cuticle at the setal root leads to an electric potential across the neuron (Weatherby and Lenz 2000; Weatherby et al. 1994). While motile prey can bend the setae via the larger flow disturbances generated by their swimming strokes, it is not clear if free-floating prey in the feeding current are hydrodynamically conspicuous (Visser 2001). It has been proposed that the feeding current could be used to aid detection of nearby particles; since the feeding current is a predictable background flow, any changes in the background flow due to the presence of prey particles in the feeding current could be detected by a copepod (Takagi and Strickler 2020; Visser 2001; Yen and Strickler 1996). Here, we study the case in which such changes arise because rigid prey particles cannot deform along with the deformations of the fluid (measured by shear or strain) in the complex flows of a beating current. Free-floating, neutrally buoyant prey particles generate this type of hydrodynamic disturbance without generating other hydrodynamic signals, such as from motility or gravitational forces. Therefore, we numerically study the flows around free-floating neutrally buoyant particles in feeding currents and their effect on the deformation of setae.

Our knowledge about whether free-floating prey entrained in the feeding current can be detected is largely dependent on microscopic observations; however, the findings of previously

reported experiments seem to contradict each other. First, it remains unclear which setae serve as the primary mechanoreceptors to detect the presence of prey entrained in the feeding current. The setae on the antennules, the primary focus in the past studies, seem most sensitive to hydrodynamic disturbances (Fields et al. 2002; Hartline et al. 1996) and motile prey are detected closest to those setae (Doall et al. 2002; Jonsson and Tiselius 1990). Nevertheless, most experiments conducted on free-floating prey observed that prey are detected closest to the setae on feeding appendages (Gonçalves and Kiørboe 2015). Second, it is unclear whether copepods are capable of detecting hydrodynamic disturbances induced by nearby prey, or instead the prey must be in contact with the seta. As summarized in table 1 of Gonçalves and Kiørboe (2015), a few studies reported that setae of copepods with $O(10^{0})$ mm prosome length have long-range sensitivity to $O(10^{-2})$ mm diameter prey (Bundy et al. 1998; Bundy and Vanderploeg 2002; Strickler 1982). However, a majority of experiments report that prey detection occurs when $O(10^{-2})$ mm diameter prey are within a few prey radii of the copepod mouthpart or tip of the feeding appendage (Gonçalves and Kiørboe 2015).

One key consideration for the long-range sensing of hydrodynamic signals is whether a copepod seta is able to distinguish the prey-induced hydrodynamic signal from its own feeding current, through a notable change in its deformation. The spatial distributions of the velocity of the background feeding current have been quantified in many experimental measurements (Catton et al. 2007; Fields and Yen 1993; Malkiel et al. 2003) and numerical simulations (Jiang et al. 1999; Jiang et al. 2002a; Jiang et al. 2002b), though not explicitly in the physical space occupied by setae. However, only a few studies (Bundy et al. 1998; Visser 2001; Yen and Okubo 2002) have addressed how prey entrainment modifies the feeding current and deformation

pattern of the seta. This may be caused by technical difficulties in, first, measuring the small prey-induced hydrodynamic disturbance relative to the background feeding current, and second, quantifying setal displacement in the feeding experiment, as very small deformations of setae are capable of initiating the predatory response. As a result, many researchers (Jiang and Strickler 2007; Kiørboe and Visser 1999; Visser 2001) have adopted simplified models which either treat the geometries of both prey and copepods as spheres (Happel and Brenner 1983), or which ignore the spatial extent of prey and copepods by representing the flows as due to a small set of multipoles, pointlike combinations of forces (Kim and Karrila 1991), which represent the flow induced by both prey and copepods in the Stokes limit, to quantify hydrodynamic disturbance sensed by the seta in feeding experiments.

For setal detection, the multipole model may often be a good representation of the flows caused by the entrained prey, if the prey radius is much smaller than the reported prey detection, hence allowing one to neglect the spatial extent of the prey. However, the spherical and multipole models are not adequate to describe the feeding current generated by the *copepod* for the following reasons. First, those models are only valid in the regime where the Reynolds number, which measures the relative importance of inertial and viscous effects in a fluid, is nearly zero. The Reynolds number is proportional to both the flow length scale and velocity. At the copepod's appendage and body length scales, the Reynolds numbers are $O(10^{-1})$ and $O(10^{0})$, respectively (Jiang et al. 2002b; Koehl and Strickler 1981; van Duren and Videler 2003), outside the range of validity of those models. Second, since it ignores the spatial extent of the copepod, the multipole model only captures the characteristics of the feeding current far away from the copepod body. However, the prey detection happens at length scale smaller than the copepod's body length, where the spatial extent and the detailed geometry of the copepod

appears to be important (Jiang and Paffenhöfer 2008; Shen et al. 2020). Last, the multipole model does not link the fluid motion with setal deformation. Recently, we (Shen et al. 2020) have addressed how the bending of setae modulates detection capabilities of copepods using hydrodynamic signals approximated as oscillating simple shear flows, but it remains unknown how the deformation patterns of setae in a feeding current is altered by the presence of nearby prey.

In this article, we focus on understanding the distance at which free-floating prey can be detected by the mechanoreceptional setae due to induced changes in the feeding current. This article consists of two sections: first, we use the immersed boundary method to numerically calculate the flow across the setae on the antennules and other feeding appendages with and without the prey entrainment. This is the flow which bends the setae, and it is the change in this flow due to the presence of prey which could possibly be sensed hydromechanically by copepods. We explicitly take into consideration of the beating strokes of the feeding appendages, though we only account for the effect of setules and setae on appendages by increasing their effective thickness. Next, we utilize the method of regularized Stokeslets and inextensible Kirchhoff rod theory to calculate the setal deformations when subjected to the bending flows obtained in the previous section. We determine how the prey-induced hydrodynamic disturbances modify the deformation patterns of the distal and proximal setae on the antennules, and predict how close to the prey the setae on the antennules must be in order to gain information about the disturbance caused by the nearby prey, depending on the sensing mechanism of the setae. Our findings are compared with previous experiments to give insights into the possible range of the prey detection distance.

Bending flow across seta

Copepod model

The geometry of our copepod model is based on copepods *Paracalanus parvus* and *Pseudocalanus sp.* in supplementary videos 1 and 3 of Tiselius et al. (2013), and described in detail in the "detailed copepod model" section in the Supplemental Information. The prosome length of the modeled copepod is assumed to be $L_b = 1$ mm (Fig. 1). Such treatment is meant to represent a typical calanoid copepod rather than any specific species. The centerline of the longest appendage pair, the antennules, is fitted to a fifth-order polynomial of arc length $L_{A1} = 1.097$ mm.

The feeding appendage geometries and beating patterns are modeled as follows. Morphological examination shows that five pairs of feeding appendages are attached to the copepod cephalosome: antennae, mandibles, maxillipeds, first maxillae, and second maxillae (Conway 2006). The second maxillae stay almost stationary (Gill and Poulet 1986) and only move occasionally to handle food particles upon detection (van Duren and Videler 2003); therefore, we neglect the presence of the second maxillae in our model. To model the other four pairs of feeding appendages, we first determine the attachment points of the roots from Tiselius et al. (2013). We then find the projected motions of these appendages from supporting video 1 of Tiselius et al. (2013). Last, we recover the three dimensional beating patterns of these feeding appendages are according to the copepod schematics as shown in fig. 2 of Koehl and Strickler (1981). Our obtained appendage motions and copepod beating strokes are animated in Videos S1 and S2a,b in the Supplemental Information, respectively.

To generate a feeding current of comparable velocity to experimental measurements, we make two assumptions. First, the beating frequency of the feeding appendages, *f*, is set to be 30

Hz in our model, within the range of common copepods' beating frequencies of 20 to 40 Hz (Koehl and Strickler 1981; Svetlichny et al. 2020; Yen and Strickler 1996). Second, the setules and setae on the feeding appendages are not explicitly accounted for in the hydrodynamic model; instead, the root diameters of all appendages are 1.5 times the values obtained from the image analysis. We found that such treatment effectively increases the contact area with surrounding fluid and generates stronger power strokes (Koehl and Strickler 1981), and produce a feeding current similar to that in experiments (see the "Validation of numerical model" section of the Supplemental Information for details).

The positions of the anterior-posterior oriented setae on the antennules are constructed based on fig. 1 of Yen and Nicoll (1990). In our model, we consider the proximal seta on the 3rd segment of the antennule and distal seta, as shown in the black lines in Fig. 1. To evaluate if the setae on the feeding appendages are sensitive to the hydrodynamic signal, we also place setae at the tips of the endopods of the antennae and maxillipeds, pointing in the direction of the appendage centerline (see Fig. 1). Similar to our previous approach (Shen et al. 2020), we assume all setae are cylindrical-shaped with length $L_{\text{seta}} = 200\ \mu\text{m}$, radius $r_{\text{seta}} = 1\ \mu\text{m}$. Results are obtained for Young's modulus of $E = 10^7\ \text{N/m}^2$ based on Yen and Okubo (2002), unless specified otherwise.

Feeding-current feeding copepods were tethered by forceps or hair for ease of microscopic observations in early experiments (Paffenhöfer and Lewis 1990; Vanderploeg et al. 1990; Yen and Strickler 1996) that quantified their behavior. In order to have a meaningful comparison with these experiments we therefore assume the body of the copepod is tethered and stationary.

Prey model

We consider a passive rigid spherical prey of the same density as the surrounding fluid. In a uniform flow, a sphere simply translates with the flow without altering it. Therefore, we expect that the free-floating prey would not generate a disturbance in a quiescent fluid or uniform flow. However, in a spatially non-uniform background flow, the finite extent of the sphere alters the flow and could be detected by the mechanoreceptional setae of copepods.

In selecting the prey size, we note that the food particles widely used in the experiments of copepod feeding on inert stimuli are non-motile algae and inert beads of diameter d varying from $O(10^0)$ to $O(10^2)$ μm (Broglio et al. 2001; Jiang and Paffenhöfer 2008; Vanderploeg et al. 1990). In our model we choose the upper limit, $d = 100$ μm and assess if the copepod setae are equipped with long-ranged hydrodynamic sensitivity to this prey type. Since the flow disturbance arises from the spatial extent of the sphere interacting with non-uniform flow, we expect smaller food to cause even less disturbance, hence be harder for copepods to detect.

Immersed boundary method

The hydrodynamics are governed by the unsteady and incompressible Navier-Stokes equations, which we solve numerically by the immersed boundary (IB) method (Peskin 1972; Peskin 2002). We adopt the constraint IB version of IBAMR (Bhalla et al. 2013) to solve for and compare the feeding current across the setae with and without presence of the prey. The setup and validation of the numerics are briefly mentioned here but described in details in the "immersed boundary method" section of the Supplemental Information

We tether the copepod at the center of the computational domain and prescribe the beating strokes of the feeding appendages. Free-floating prey are treated as (net) force- and torque-free particles in IB simulations, allowing them to drift in the feeding current. The fluid is at rest at t =

196 0, and accelerates due to the constraints provided by the no-slip boundary conditions specified by
197 the copepod and prey geometry and motion. Similar to the approximations made in the arthropod
198 filiform hair model (Humphrey et al. 1993) and our previous approach (Shen et al. 2020), we
199 assume that the setae are far from each other and have negligible disturbance to the feeding
200 current, and hence we do not explicitly include setae filaments as part of the immersed copepod.
201 The flow profile obtained from the numerical model is validated by comparing the time-averaged
202 steady-state flow with that measured experimentally in Fields and Yen (1997).

203 **Bending flow across feeding appendage setae**

204 Here we evaluate how the bending flows across the setae on the feeding appendages and the
205 antennules are affected by free-floating prey. We find that there is little difference in flow with
206 and without free-floating prey at setal locations on feeding appendages.

207 In our numerics, we first let the copepod's feeding appendages beat for 60 cycles so that the
208 bending flows across all setae are within 2% of their corresponding steady state values (see the
209 "steady state test" section in the Supplemental Information). We then center a free-floating prey
210 at Point A and reset the time to be $t = 0$. Point A (Fig. 1) is on the sagittal plane of the copepod
211 approximately 0.5 mm in front of the feeding appendages. Since the prey is force- and moment-
212 free, it is entrained in the feeding current and moves towards the feeding appendages over time,
213 as shown by the prey trajectory in Fig. 2a. In Figs. 2b and 2c, we plot the distance, *D*, from the
214 prey center to the setae on the maxilliped and the endopod of the antenna as a function of time,
215 respectively.

216 To analyze the prey-induced disturbance sensed by the setae, we evaluate the velocities of
217 the bending flows along the setal axis relative to their corresponding setal root velocities,

$\Delta\mathbf{u}(s,t) = \mathbf{u}(s,t) - \mathbf{u}(0,t)$, where $s \in [0, L_{\text{seta}}]$ is a Lagrangian parameter along the centerline of the seta, with $s = 0$ at the setal root. In Figs. 2d and 2e, we plot the *x*, *y* and *z* components of the instantaneous bending flows across the setae on the maxilliped and the endopod of the antenna with and without a free-floating prey when their corresponding distances to the prey are the shortest. The shortest distance from the prey center to the seta on the endopod of the antenna is 0.265 mm (equivalent to 5.3 prey radii), occurring at time $t/T = 25.44$ (refer to Fig. 2c), and the shortest distance from the prey to the seta on the maxilliped is even smaller (0.163 mm, equivalent to 3.3 prey radii), occurring at time $t/T = 21.91$ (refer to Fig. 2b). We find that the presence of the prey induces negligible difference in the sensed flow across these seta (note that the dashed lines coincide with the solid lines in Figs. 2d,e). The limited change in flow across the setae on feeding appendages is consistent with the conclusion reached by Gonçalves and Kiørboe (2015), which implies that feeding appendage setae may not be designed for prey detection through hydromechanical reception, as opposed to direct contact. As might be expected, we found that free-floating prey starting farther from the feeding appendages produce even less difference in flow across these setae (data not shown). Therefore in the remainder of this paper we focus on the setae on the antennule instead.

Bending flow across the setae on the antennule

Without the presence of the prey

First we evaluate the feeding current flow without prey across the setae on the antennule. The flow velocities at the roots of these setae should be zero due tethered boundary condition applied on the copepod. However, a known drawback of the constraint IB method is that the boundary conditions are satisfied only approximately, leading to a mild penetration of the flow through the copepod body (Kallemov et al. 2016).

241 To resolve this issue, we adjust the positions of the setae on the antennule in the *x* direction
242 (Fig. 1a) so that the setal root is about one computational grid into the antennule object, where
243 the calculated feeding current is the smallest. At these root locations, the feeding current is 5.7%
244 (13.8%) of the maximum magnitude of the flow across the corresponding distal (proximal) seta
245 on the antennule. To correct for this residual flow we use the quantity $\Delta\mathbf{u}(s,t)=\mathbf{u}(s,t)-\mathbf{u}(0,t)$
246 to evaluate the velocities of the bending flows along the centerline *s* of the distal and proximal
247 setae on the antennule.

248 The steady-state bending flow across these setae is highly oscillatory (refer to Fig. S6 in the
249 Supplemental Information for the plot of the steady-state $\Delta\mathbf{u}(s,t)$ across the distal and proximal
250 setae at selected times over one beating cycle). This is characteristic of all the feeding current
251 flows we examine, since they are generated by oscillatory movement of the feeding appendages.
252 Therefore, in what follows we quantify the bending flow by decomposing it into time-averaged
253 and oscillatory components during the *N*-th beating stroke ($(N-1)T \le t < NT$),

254 $$\Delta\mathbf{u}(s,t) = \Delta\mathbf{u}_{\text{avg}}(s,NT) + \Delta\mathbf{u}_{\text{osc}}(s,t), \qquad (1)$$

255 where $\Delta\mathbf{u}_{\text{avg}} = (1/T)\int_{(N-1)T}^{NT} \Delta\mathbf{u}\,dt$ is the time-averaged velocity at centerline position *s* over one
256 oscillation cycle, and $\Delta\mathbf{u}_{\text{osc}}$ represents the oscillatory velocity component of the bending flow.

257 *Free-floating prey near the distal seta*

258 In this section, we show that free-floating prey hardly affect the feeding current at the distal
259 setal locations unless they are quite close (less than 10 prey radii) to the antennules. After the
260 flow reaches steady state, we reset the time to be $t=0$ and start a free-floating at Point B (Fig.
261 1), in front of the distal of the left antennule and 0.5 mm from its centerline. Near the antennule,

the hydrodynamic interaction between the antennules and the free-floating prey can be seen to alter the prey trajectory (Figs. 3a-c). We show the time-averaged bending flows, $\Delta\mathbf{u}_{avg}$, across the left distal seta at four typical beating cycles with and without the free-floating prey in Figs. 3d-h. From these results we make the following observations:

First, in the 1st beating cycle ($0 \le t/T < 1$), when the free-floating prey is 0.5 mm (10 prey radii) from the centerline of the antennule (Figs. 3a,b), we did not observe any difference in the average flow across the distal seta $\Delta\mathbf{u}_{avg}$ due to the presence of the free-floating prey (note the solid and dashed lines coincide in Fig. 3d).

Second, in the 61st beating cycle, when the prey appears to be closest to the distal setal tip (0.160 mm away, equivalent to 3.2 prey radii from setal tip and 5.5 prey radii from the centerline of the antennule, Figs. 3a,b), we only observe a small change in the *y* component of $\Delta\mathbf{u}_{avg}$ (compare the solid and dashed lines in the middle panel of Fig. 3e). This is due to the fact that our hydrodynamic model neglects the presence of the distal setae and its hydrodynamic interaction with the prey; the change in $\Delta\mathbf{u}_{avg}$ across the distal seta is induced by the relatively weak hydrodynamic interaction of the prey and the antennule.

Third, in the 91st beating cycle, when the prey is 0.171 mm (3.4 prey radii) from the centerline of the antennule (Figs. 3a,b), we observe the largest difference in $\Delta\mathbf{u}_{avg}$ across the distal seta (compare the solid and dashed lines in Fig. 3f). In comparison, the free-floating prey initiated at Point A does not induce a noticeable change in the bending flow across the setae on feeding appendages when the distance from the prey to the maxilliped is about the same as the case here (3.4 prey radii). This demonstrates that the distal seta on the antennule has a higher

hydrodynamic sensitivity than feeding appendage setae, aided by the small magnitude of the feeding current across the distal seta, which creates a quiet hydrodynamic sensing environment.

Fourth, in the 112th beating cycle, when the prey is closest to the centerline of the antennule (0.138 mm away, equivalent to 2.8 prey radii, Figs. 3a,b), we find that the time-averaged prey-induced disturbance is smaller than that at the 91th beating cycle (compare the differences of the solid and dashed lines in Fig. 3f and in Fig. 3g). Thus there is no guarantee that the largest difference in bending flow occurs when the prey is closest to the centerline of the antennule.

Finally, in the last (140th) cycle of our simulation, when the prey is 0.183 mm (equivalent to 3.6 prey radii) from the centerline of the antennule, we do not observe any difference in the time-averaged bending flow with and without the prey (Fig. 3h).

Next we examine the oscillatory portion of the flow across the distal seta $\Delta\mathbf{u}_{\mathrm{osc}}$. In Fig. S7a of the Supplemental Information, we plot $\Delta\mathbf{u}_{\mathrm{osc}}$ across the distal seta with and without the presence of the prey during the 91st cycle (when the difference in $\Delta\mathbf{u}_{\mathrm{avg}}$ is the largest). In general, the oscillatory velocity component has the same order of magnitude as the time-averaged ones (compare the horizontal scales of Fig. 3f with Fig. S7a). This oscillatory flow velocity has not been revealed by the previous numerical models (Bundy et al. 1998; Jiang et al. 1999; Jiang et al. 2002a) that either treat the hydrodynamic effect of the beating appendages as due to constant point forces, or assume the copepod swims at a constant speed; hence only capturing the time-averaged feeding current over a cycle of beating stroke. It is often argued that by analogy with the flow over an infinite oscillatory plate, oscillatory flows caused by the appendages should decay over a length scale set by viscous diffusion, $L_{\mathrm{d}} = \sqrt{\mu/(\pi\rho f)}$, which

for appendage oscillations of frequency $f = 30$ Hz is $L_d \approx 103$ μm (Jiang et al. 2002b). According to this argument, the oscillatory flow should have mostly decayed at the distance of the setae on the antennules. Interestingly, our full flow solution shows that the flow does not decay as much as expected, and that appreciable oscillatory component of the feeding current can be observed around the distal seta, more than 1 mm from the feeding appendages. Comparing velocities of bending flows across the distal seta with and without prey, we find that the oscillatory flow is nearly the same at all eight selected time frames over a cycle, so it is not much affected by the presence of prey. Since the presence of prey largely only affects the time averaged flows around the setae on the antennules, in the remainder of the paper we focus on the time-averaged feeding current, $\Delta\mathbf{u}_{avg}$, rather than the oscillatory flows.

To summarize, the hydrodynamic disturbance induced by free-floating prey at the distal seta induces small changes in the time-averaged background feeding current, with a notable change in the bending flow occurring when the prey is less than 5.5 prey radii away from the antennule. Note also that although the change in bending flow due to the prey-induced hydrodynamic distance is small in this example, the prey requires about 110 cycles ($\approx$ 3.3 s) to travel across the antennule, which gives the distal seta a relatively long time to sense its presence.

Free-floating prey near the proximal seta

Now, after the flow reaches steady state, we reset the time to be $t = 0$ and start a free-floating prey at Point C (Fig. 1) in front of the proximal of the left antennule and 0.5 mm from its centerline. The prey trajectory relative to the centerline of the antennule and proximal (distal) seta is shown in Figs. 4a,b (Figs. 5a,b). Fig. 4c plots the distance from prey center to the centerline of the antennule over time. The prey-induced hydrodynamic disturbance is expected to

be stronger due to stronger flows and spatial variation in flows near the proximal compared to near the distal of the antennule. In this case, in addition to the proximal seta, the distal seta has a chance to sense the prey-induced flow disturbance, even though Point C is farther from the distal seta than Point B. Therefore, we consider the bending flow across both setae.

Similar to the case with prey near the distal of the antennule, we observe that the oscillatory portion of the flow across the proximal seta is hardly altered by the presence of the prey (Fig. S7b in the Supplemental Information). Consequently, we show the *x*, *y* and *z* components of the time-averaged bending flows, $\Delta\mathbf{u}_{avg}$, across the proximal and distal setae at four typical beating cycles in Figs. 4d to 4g and Figs. 5c to 5f, respectively, and make the following observations:

First, during the 1st cycle, when the prey just departs from Point C (Figs. 4a,b and Figs. 5a,b), we find no difference in the bending flow across the proximal and distal setae with and without the presence of prey (note that the solid and dashed lines coincide in both Figs. 4d and 5c). This demonstrates that although the prey-induced disturbance near the proximal is larger than that near the distal of the antennule, both the proximal and distal setae are not capable of sensing free-floating prey when it is 10 prey radii away from the antennule.

Second, during the 17th cycle, when the prey is closest to the centerline of the antennule (0.153 mm away, equivalent to 3.1 prey radii, Figs. 4a,b and 5a,b), we observe some difference in $\Delta\mathbf{u}_{avg}$ across the proximal seta with and without the presence of the prey (compare the solid and dashed lines in Fig. 4e) but did not find any noticeable difference for the distal seta (Fig. 5d).

Third, the largest difference in the sensed flow across the proximal (distal) seta occurs at the 19th (23rd) beating cycle, in which the distance from the prey to the centerline of the antennule is about 0.189 mm (0.395 mm), equivalent to 3.8 prey radii (7.9 prey radii). Compare the solid

348 and dashed lines in Figs. 4f and 5e. This again shows that being closest to the antennule does not
349 guarantee the largest difference in the bending flow. Both the second and third observations
350 suggest that there may be a few beating cycles of delay between for the distal seta to receive prey
351 information compared to the proximal seta.

352 Finally, in the last (30th) cycle of our simulation, when the prey is 0.567 mm (equivalent to
353 11.3 prey radii) from the centerline of the antennule, we do not observe any difference in the
354 time-averaged bending flow with and without the prey (note the solid and dashed lines coincide
355 in Figs. 4g and 5f).

356 To summarize, we see that the prey entrained at the proximal region of the antennule
357 generates a larger flow disturbance and is relatively easily sensed by the setae on the antennule
358 when the prey is about 3 prey radii from the centerline of the antennule. This example
359 demonstrates that prey can sometimes induce differences in the bending flows on multiple setae.
360 Therefore, if the prey-induced hydrodynamic disturbance causes the neurons on more than one
361 seta to fire, the prey detection may involve the coordination of the setal array on the antennule, in
362 agreement with previous hypotheses (Fields 2014; Yen and Nicoll 1990). Last, we note that
363 although the change in bending flow could be significant, the prey only requires 19 cycles ($\approx$
364 0.6 s) to move across the antennule, giving the proximal seta a relatively short time to sense its
365 presence.

366 ***Deformation of seta***

367 In this section, we analyze the change in the setal deformation due to the hydrodynamic
368 disturbance induced by prey to evaluate if the setae are sensitive to their presence. To relate the
369 hydrodynamic signal received by the setae on the antennule with their neurological responses,

we solve for the deformation of the seta when subjected to the bending flows described in the previous section. In previous work investigating the deformation of seta due to background shear flows, we solved for the time-dependent setal shape by assuming small two-dimensional setal deformations, and balancing elastic forces obtained from Euler beam theory against the hydrodynamic forces obtained from resistive force theory (Shen et al. 2020). In this paper, we must move beyond the Euler beam description of elastic forces, since the setal deformation is not necessarily small, and the flow and bending are inherently three-dimensional. Therefore we apply the more general Kirchhoff rod theory and method of regularized Stokeslets to solve for large scale setal deformations in three-dimensional feeding current flows.

Method

The method to solve for the setal deformation is as follows. We consider a seta which is straight at time $t = 0$ and deforms when subjected to the feeding current obtained in the "bending flow across the setae on the antennule" section. At each cross section of the seta specified by centerline position s, we define a set of orthonormal basis vectors $\left[\mathbf{d}_1(s,t), \mathbf{d}_2(s,t), \mathbf{d}_3(s,t)\right]$ to express the orientation of the filament cross section, where the unit tangential vector $\mathbf{d}_3 = \partial_s \mathbf{X} / \left|\partial_s \mathbf{X}\right|$, while $\mathbf{d}_1$ and $\mathbf{d}_2$ are material unit vectors spanning the cross section. As a thin filament, the internal force and torque $\mathbf{F}(s,t)$ and $\mathbf{N}(s,t)$, arising from the setal deformation are governed by Kirchhoff rod theory (KRT) (Jabbarzadeh and Fu 2018; Lim et al. 2008; Olson et al. 2013), given by

$$\partial_s \mathbf{F} + \mathbf{f} = 0, \tag{2}$$

$$\partial_s \mathbf{N} + \mathbf{d}_3 \times \mathbf{F} + \mathbf{n} = 0, \tag{3}$$

where $\mathbf{f}(s,t)$ and $\mathbf{n}(s,t)$ are the hydrodynamic force and torque distribution exerted by fluid along the setal centerline s, respectively. As the setal deformation is dominated by bending rather than stretching (Fields et al. 2002), we utilize the inextensible version of the KRT (Jabbarzadeh and Fu 2020) which implies that $\left|\partial_s \mathbf{X}\right| = 1$, and $N_i = \mathbf{N}\cdot\mathbf{d}_i \ (i = 1, 2, 3)$ can be expressed as

$$N_1 = EI\left(\partial_s \mathbf{d}_2\right)\cdot\mathbf{d}_3, \tag{4}$$

$$N_2 = EI\left(\partial_s \mathbf{d}_3\right)\cdot\mathbf{d}_1, \tag{5}$$

$$N_3 = GJ\left(\partial_s \mathbf{d}_1\right)\cdot\mathbf{d}_2, \tag{6}$$

where $I = \pi r_{\text{seta}}{}^4/4$ and $J = \pi r_{\text{seta}}{}^4/2$ are the planar and polar second moment of seta, respectively. The seta is treated as isotropic with Poisson's ratio $\upsilon = 0.3$ (Yen and Okubo 2002), hence $G = E/\left[2(1+\upsilon)\right]$.

Due to the small length and velocity scales of the flow past seta ($r_{\text{seta}} = 1$ μm and $\left|\mathbf{u}(s,t)\right| < \mathrm{O}\left(10^0\right)$ mm/s), the Reynolds number is small enough that fluid motion is governed by the Stokes equations:

$$-\nabla p + \mu\nabla^2\mathbf{u} + \mathbf{f}_b = 0, \tag{7}$$

$$\nabla\cdot\mathbf{u} = 0. \tag{8}$$

Here we couple the Eqs. (2) and (3) with Eqs. (7) and (8), and apply the boundary conditions that the seta is fixed and clamped at its root ($\partial_t \mathbf{X}\big|_{s=0} = \partial_s \mathbf{X}\big|_{s=0} = \mathbf{0}$) and force- and moment-free at the other end ($\mathbf{F}\big|_{s=L_{\text{seta}}} = \mathbf{N}\big|_{s=L_{\text{seta}}} = \mathbf{0}$). Our numerical scheme implements the method of regularized Stokeslets (MRS) (Cortez 2001; Cortez et al. 2005) to find the hydrodynamic forces on the seta, and then solves Eqs. (2) and (3) for the deformed shape of the seta. Details of our

numerical scheme to implement the MRS (Hyon et al. 2012; Martindale et al. 2016) and KRT (Jabbarzadeh and Fu 2020) and convergence test results are shown in the "numerical scheme for setal deformation" section of the Supplemental Information, but briefly, we uniformly place a total number of N regularized Stokeslets on the surface of the seta with physical coordinates X_n $(n = 1, 2, ..., \mathrm{N})$. For each seta, the setal velocity $\mathbf{v}(s,t)$ at $\mathbf{X}(s,t)$ can be evaluated by using

$$\mathbf{v}(s,t) = \partial_t \mathbf{X} = \Delta\mathbf{u}(s,t) + \sum_{n=1}^{\mathrm{N}} \mathrm{S}\left(\mathbf{X}, \mathrm{X}_n, \varepsilon\right) \mathrm{F}_n(t), \tag{9}$$

where $\Delta\mathbf{u}(s,t)$ is the bending flow (obtained in the "bending flow across the setae on the antennule" section) prescribed at position *s* and time *t* without the presence of the seta, and $\mathrm{F}_n(t)$ are the components of the strength of the regularized Stokeslet at position X_n and time *t*; the regularized Stokeslet kernel S is defined in Eq. S6 of the Supplemental Information.

Setae are more sensitive to time-averaged feeding current

Here we solve for the shape of the setal centerline, $\mathbf{X}(s,t)$, for the distal seta when placed in the time-dependent bending flows. We use the magnitude of the setal tip displacement, defined as

$$\ell(t) = \left|\mathbf{X}(L_{\text{seta}}, t)\right|, \tag{10}$$

and the magnitude of the setal root curvature, defined as

$$\kappa(t) = \left| \left. \frac{\partial^2 \mathbf{X}(s,t)}{\partial s^2} \right|_{s=0} \right|, \tag{11}$$

to relate the hydromechanical signal received by the seta (bending flow) with its neurophysiological response (electric potentials). The tip displacement has been often used in the previous experiments to estimate the angular displacement of seta (Fields et al. 2002; Yen et al.

1992). The root curvature has been hypothesized to be positively correlated with the chance of sensing environmental signals, as discussed in Shen et al. (2020). In short, root curvature is associated with shear displacement of the cuticle relative to the microtubule-filled dendrites extending along the antennule and anchored to the inner wall of its cuticle at the setal root (fig. 5 of Shen et al. (2020)), opening the mechano-gated microchannels perforating the dendritic membrane and leading to the transduction of mechanical signal into neurophysiological signal.

To determine the effect of the bending flow on the mechanical response of the seta, we first consider the deformation pattern, tip displacement and root curvature of the distal seta when subjected to the bending flow in the absence of prey (described in Fig. S6a in the Supplemental Information). In Figs. 6a,b, we plot the distal setal shape at four selected time frames within a beating cycle, after the time-averaged setal shape reaches steady state. We find that although the magnitude of the oscillatory bending flow component ($|\Delta\mathbf{u}_{\mathrm{osc}}|$) across the distal seta is of the same order as that of the time-averaged bending flow component ($|\Delta\mathbf{u}_{\mathrm{avg}}|$) the seta seems to respond much more strongly to the time-averaged component, bending towards a fixed direction while having a relatively small amplitude of oscillation.

To quantify the setal deformation, we plot magnitudes of the tip displacement (ℓ) and root curvature (κ) of the distal seta over 15 beating cycles in Figs. 6c,d. We characterize ℓ and κ at the *N*-th beating cycle by using their corresponding time-averaged responses over one beating cycle of period *T*, denoted by

$$\ell_{\mathrm{avg}} = \frac{1}{T}\int_{(N-1)T}^{NT} \ell \,\mathrm{d}t \tag{12}$$

and

$$\kappa_{\text{avg}} = \frac{1}{T}\int_{(N-1)T}^{NT} \kappa \mathrm{d}t \,, \tag{13}$$

and peak-to-peak amplitudes, denoted by ℓ_{pp} and κ_{pp} (see Figs. 6c,d). The time-averaged setal responses, ℓ_{avg} and κ_{avg}, are caused by the time-averaged bending flow component $\Delta\mathbf{u}_{\text{avg}}$, while the fluctuations around the average are induced by the oscillatory bending flow component $\Delta\mathbf{u}_{\text{osc}}$. When the response of the distal seta reaches steady state, we find from Figs. 6c and 6d that ℓ_{avg} is 2.86 times larger than ℓ_{pp}, and that κ_{avg} is 1.45 times larger than κ_{pp}, in accord with the qualitative observation in the previous paragraph that the seta responds mostly to the time-averaged flow. This result is also consistent with our previous work (Shen et al. 2020), which explains why the bending response of setae behaves as a low-pass filter to flow velocity signals.

Our findings here have two implications on the prey detection of the feeding-current feeding copepods. First, at the most common range of beating frequencies ($20\ \text{Hz} \le f \le 40\ \text{Hz}$), the effect of the oscillatory flow component on the hydrodynamic sensing is small. As the free-floating prey does not cause notable changes in the oscillatory flow components (see Fig. S7 in the Supplemental Information), the bending mechanism of the setae filters out less important hydrodynamic signals. Second, the time-averaged flow component is most important for prey detection. The presence of nearby prey does cause notable changes to the time-averaged flow across the setae (see Figs. 3f, 4f and 5e). The setal bending response, being a low-pass velocity filter (Shen et al. 2020), preserves the magnitude of this time-averaged signal and increases the chance of prey detection.

Setal deformation due to free-floating prey

Free-floating prey near the distal seta

473 We further examine how the proximal and distal setae respond to free-floating prey of
474 diameter 100 μm. We first consider the case in which the prey approaches the distal seta from
475 point B along the trajectory shown in Figs. 3a,b. Our results for setal bending are presented in
476 terms of three different prey detection criteria. The exact type of bending signal which leads to
477 copepod response remains unknown, and the different prey detection criteria correspond to
478 different possibilities.

479 The first criterion supposes that prey detection of copepods is related to the absolute change
480 in the tip displacement or root curvature of the seta due to the presence of the prey, $\left|\Delta\ell_{\text{avg}}\right|$ or
481 $\left|\Delta\kappa_{\text{avg}}\right|$, respectively defined as

482 $$\left|\Delta\ell_{\text{avg}}\right| = \left|\ell_{\text{avg}}\left(NT\right)-\ell\left(0\right)\right| \tag{14}$$

483 and

484 $$\left|\Delta\kappa_{\text{avg}}\right| = \left|\kappa_{\text{avg}}\left(NT\right)-\kappa\left(0\right)\right|. \tag{15}$$

485 The former has been widely used to relate the strength of external stimulus with setal
486 deformation (Fields et al. 2002; Yen et al. 1992), while the latter has been proposed by us to be
487 directly related to the physiological response of the copepods (Shen et al. 2020).

488 The second criterion supposes that the copepod seta adapts in sensitivity to the average level
489 of background signal caused by the feeding current. The seta only responds to the *relative*
490 change in deformation with respect to the background, expressed as

491 $$\mathrm{R}_{1,\text{disp}} = \frac{\left|\Delta\ell_{\text{avg}}\right|}{\ell_{\text{avg,w/o}}} \tag{16}$$

492 and

493 $$R_{1,curv} = \frac{\left|\Delta\kappa_{avg}\right|}{\kappa_{avg,w/o}} \quad (17)$$

494 if the tip displacement and root curvature are used, respectively, where $\ell_{avg,w/o}$ ($\kappa_{avg,w/o}$)
495 represents the magnitude of the time-averaged tip displacement (root curvature) without the
496 presence of the prey. Larger $R_{1,disp}$ and $R_{1,curv}$ are more likely to lead to prey detection.

497 The third criterion supposes that prey detection happens only when the change in
498 hydrodynamic signal induced by the prey can be distinguished from the time-dependent
499 fluctuations in signal due to the feeding current. We define this prey detection criterion in terms
500 of the setal tip displacement ratio as

501 $$R_{2,disp} = \frac{\left|\Delta\ell_{avg}\right|}{\ell_{pp,w/o}}, \quad (18)$$

502 and in terms of the root curvature ratio as

503 $$R_{2,curv} = \frac{\left|\Delta\kappa_{avg}\right|}{\kappa_{pp,w/o}}, \quad (19)$$

504 where $\ell_{pp,w/o}$ and $\kappa_{pp,w/o}$ are the peak-to-peak amplitudes of the tip displacement and root
505 curvature without the prey, respectively. It seems likely that copepods would not gain an
506 advantage by responding to these predictable fluctuations, so we hypothesize that the copepod
507 seta is more likely to sense the presence of the prey for $R_{2,disp} > 1$ or $R_{2,curv} > 1$.

508 In Figs. 7a and 7b, we show the magnitude of the average tip displacement (ℓ_{avg}) and root
509 curvature (κ_{avg}), respectively, as well as vertical bars representing their peak-to-peak ranges (ℓ_{pp}
510 or κ_{pp}), along with the distance from the prey center to the centerline of the antennule over the

prey trajectory. Only results for the distal seta are presented, as the small hydrodynamic disturbance induced by the free-floating prey does not cause any notable change in the deformation pattern of the proximal seta.

We use the three aforementioned prey detection criteria to evaluate the hydrodynamic sensitivity of the distal seta. First, the detection of free-floating prey through absolute changes in the tip displacement or root curvature of the setae is feasible but highly unlikely. We find that the maximum changes in ℓ_{avg} and κ_{avg} are 0.32 nm and 1.2 m^{-1}, respectively. According to past experiments performed on copepods, the threshold displacement to trigger setal response is at least 10 nm (Yen et al. 1992). Second, hydromechanical detection relative to average bending through $R_{1,disp}$ or $R_{1,curv}$ is feasible. The maximum $R_{1,disp}$ and $R_{1,curv}$ are 5.3% and 5.2%, respectively, which may give the copepod some information about the presence of prey. Last, detection relative to oscillatory background bending through $R_{2,disp}$ and $R_{2,curv}$ is unlikely; the peak-to-peak amplitudes of the tip displacement and root curvature without the prey are much larger than the changes in the corresponding time-averaged quantities.

Free-floating prey near the proximal seta

We next consider the case in which the prey approaches the proximal seta on the antennule from point C along the trajectory shown in Figs. 4a,b. We expect that the stronger prey-induced disturbance in Figs. 4 and 5 may cause more changes in the deformation of each seta. In Fig. 8, we show the magnitude of the average tip displacement (ℓ_{avg}) and root curvature (κ_{avg}), for both the distal and proximal seta, as well as vertical bars representing their peak-to-peak ranges (ℓ_{pp}

or κ_{pp}), along with the distance from the prey center to the centerline of the antennule over the prey trajectory.

The tip displacement and root curvature of both setae follow similar trends. First, in the first beating cycle, we find that the prey, at Point C and 0.50 mm to the antennule, does not cause any notable changes in ℓ_{avg} and κ_{avg} of the setae. This is due to the fact that even in the strong flow near the proximal of the antennule, the hydrodynamic disturbance induced by free-floating prey is too weak to be sensed by the nearest seta 10 prey radii away. Second, we note that the changes in tip displacement and root curvature induced by the entrained prey are not necessarily larger as the prey moves closer to the antennule. When approaching the proximal (distal) seta, the prey alters the surrounding current and reduces the deformation amplitude of distal (proximal) seta around the 15th (21st) beating cycle. Last, the maximum responses of the copepod setae may not occur at the shortest distance to the prey. This can be easily seen from the distal seta, for which the maximum changes in deformation occur at the 24th cycle, when the prey has travelled past the centerline of the antennule.

We again use the three prey detection criteria (Eqs. (14) to (19)) to assess whether free-floating prey near the proximal of the antennule can be detected. For the distal seta, we find that maximum changes in ℓ_{avg} and κ_{avg} are very similar to those for prey near the distal of the antennule (compare Fig. 8c with Fig. 7a, and Fig. 8d with Fig. 7b). Therefore, we reach the same conclusions: prey detection through changes in setal deformation relative to average background bending is feasible, while detection through absolute changes in setal deformation and relative to oscillatory background bending is unlikely. For the proximal seta, we find that the maximum change in ℓ_{avg} and κ_{avg} are significantly larger, while the maximum $R_{1,disp}$ and $R_{1,curv}$ are both

around 5%. Thus detection of absolute changes in setal deformation and relative to average background bending is possible, while detection through changes in setal deformation relative to oscillatory background bending remains unlikely.

Discussion

In this study, we have developed a numerical model that evaluates how the setae of a feeding-current feeding copepod respond to the hydrodynamic disturbance induced by the prey entrainment. We used the immersed boundary method to compute the feeding current induced by a tethered copepod by prescribing the beating strokes of its feeding appendages. We determined the changes in bending flows across the setae caused by free-floating prey. We found that the time-averaged component of the prey-induced flow disturbance is more relevant to the hydromechanical reception of copepods. The setae at the feeding appendage region suffer from the strongest background feeding current, and have the least relative change in bending flow induced by nearby prey. On the other hand, the distal seta on the antennule is subjected to the least background current, and is most sensitive to small changes in the prey-induced bending flow.

We used a relatively large prey size (100 μm diameter) since smaller prey required finer numerical meshes and were not computationally feasible. However, our results can be used to gain insights into the sensed current caused by smaller free-floating prey in reality. In this study, 100 μm diameter free-floating prey do not cause any notable change in the bending flow across the setae on the antennule until the distance from the prey to the centerline of the antennule is less than 5 prey radii from the antennule. To estimate the prey detection distance for a prey of smaller radius (d/2), we follow the approach of Visser (2001) to express the hydrodynamic

disturbance of a neutrally buoyant prey as $\dot{\varepsilon}(d/2)^3/r^2$, at a distance r from the prey in a background flow characterized by strain rate $\dot{\varepsilon}$. Assuming the same strain rate and the same disturbance magnitude needed for detection, this implies that detection distance scales as $(d/2)^{3/2}$. This suggests that if the setae on the antennule are capable of detecting free-floating prey, the prey of 5, 10 and 25 μm in radius will be detected within 1.6, 2.2 and 3.5 prey radii from the antennule, respectively.

We have evaluated the changes in deformation patterns of the setae on the antennule relative to those due to the background current, by coupling the method of regularized Stokeslets and inextensible Kirchhoff rod theory. We find that the copepod setae, as low pass velocity filters, are most sensitive to the time-averaged flow component of the feeding current. We proposed three prey detection criteria based on the changes in either tip displacement or root curvature to determine the copepod's prey detection capability. First, if characterized as an absolute change sensor, the copepod seta nearest to the prey is responsible for the prey detection. The small change in the deformation of the distal seta indicates that this detection mechanism is unlikely for the distal seta. Second, if characterized as a relative change sensor, the distal seta may be equipped with a long-ranged hydrodynamic sensitivity that assists the detection of the free-floating prey at the proximal region of the antennule. Third, if prey detection requires the prey-induced signal to be completely distinguished from the background fluctuations, both setae on the antennule have very short-range hydrodynamic sensitivity that requires the prey to touch or nearly touch the seta before being sensed.

Our three prey detection criteria imply different sensory mechanisms of the setae. Our results suggest that the mechanism of signal transduction can be better understood through experiments

that distinguish these criteria, which would ultimately shed light on how copepods sense their surroundings in the presence of not only self-generated noise such as the feeding current, but also environmental noise. For example, our results suggest that the proximal and distal setae have different amounts of changes in absolute magnitude compared to relative magnitude of bending and curvature. Both absolute and relative deflections of setae could be measured experimentally while observing triggering of physiological and behavioral responses of copepods, to see which is more important for sensing. If relative signals are more correlated with response, this implies that the distal setae are likely to be more important for sensing, even for particles that are closer to proximal setae. Interestingly, if $R_{2,disp}$ or $R_{2,curv}$ need not be greater than 1 for physiological and behavioral responses to be triggered, this implies that the triggering mechanism is somehow able to filter out the oscillatory signal of feeding current, which could be an important adaptation to allow sensing in the presence of noise.

We can also use the three prey detection criteria to assess the distance dependence of detection of free-floating prey. We find that free-floating prey generate minimal flow disturbances and are relatively hydrodynamically inconspicuous to copepods. They do not induce any changes in the responses of the distal and proximal seta unless they are less than 10 and 5.5 prey radii away from the antennule, respectively. The short-ranged sensitivity of the setae on the antennule to free-floating prey may explain why most copepod feeding experiments using free-floating prey report that prey are missed by the setae and are detected upon reaching the vicinity of the feeding appendages (Gonçalves and Kiørboe 2015).

Finally, we point out the limitations of our current model and provide suggestions for future work. First, the copepod in our model is tethered in space, which only happens in laboratory setups. The prescribed swimming strokes of the feeding appendages do not guarantee that the

force- and moment-free conditions are satisfied automatically for a free-swimming and gravity-tethered copepods in nature, which might be investigated in further work. Second, the numerical method adopted in the our IB method relies on the fractional-step approach, in which the no-slip boundary condition is satisfied approximately and leads to a penetration of the flow into the copepod body and appendages. At zero to intermediate Reynolds number region, the prescribed boundary conditions could instead be satisfied exactly by using a direct forcing and unsplit method such as in Kallemov et al. (2016) and Usabiaga et al. (2017). Third, the setal deformation is solved in two steps, neglecting the presence of the setae filaments while determining the bending flows, then solving for setal deformation in the determined bending flow. Thus the accuracy of the setal deformation can be improved by incorporating its hydrodynamic effect on the flow through a finite element treatment and directly finding its deformation in the IB method. Last, we have focused on the sensing of hydrodynamic disturbances caused by the mismatch between the rigid body motion of a prey particle and the deformational flows of feeding currents. Another possible mechanism of sensing may be the phase mismatch of non-neutrally-buoyant particles with the oscillatory feeding current (Giuffre et al. 2019). In that case, additional hydrodynamic signals arising from the net force exerted on the fluid by the weight of the particle are unavoidable and could also be sensed by the copepod. Likewise, motile prey could be sensed not only through the disturbance to feeding current studied here, but also by sensing the flows caused by their motility. Detection of such particles that produce multiple hydrodynamic signals is worthy of future investigation.

Reference

642 Bhalla, A. P. S., R. Bale, B. E. Griffith, and N. A. Patankar. 2013. A unified mathematical
643 framework and an adaptive numerical method for fluid–structure interaction with rigid,
644 deforming, and elastic bodies. J. Comput. Phys. **250:** 446–476.
645 Broglio, E., M. Johansson, and P. R. Jonsson. 2001. Trophic interaction between copepods and
646 ciliates: effects of prey swimming behavior on predation risk. Mar. Ecol. Prog. Ser **220:**
647 179-186.
648 Bundy, M. H., T. F. Gross, H. A. Vanderploeg, and J. R. Strickler. 1998. Perception of inert
649 particles by calanoid copepods: behavioral observations and a numerical model. J.
650 Plankton Res. **20:** 2129-2152.
651 Bundy, M. H., and H. A. Vanderploeg. 2002. Detection and capture of inert particles by calanoid
652 copepods: the role of the feeding current. J. Plankton Res. **24:** 215-223.
653 Catton, K. B., D. R. Webster, J. Brown, and J. Yen. 2007. Quantitative analysis of tethered and
654 free-swimming copepodid flow fields. J. Exp. Biol. **210:** 299-310.
655 Conway, D. V. P. 2006. Identification of the copepodite developmental stages of twenty-six
656 North Atlantic copepods. Marine Biological Association of the United Kingdom.
657 Cortez, R. 2001. The method of regularized Stokeslets. SIAM J. Sci. Comput. **23:** 1204–1225.
658 Cortez, R., L. Fauci, and A. Medovikov. 2005. The method of regularized Stokeslets in three
659 dimensions: analysis, validation, and application to helical swimming. Phys. Fluids **17:**
660 031504.
661 Doall, M., J. R. Strickler, D. M. Fields, and J. Yen. 2002. Mapping the free-swimming attack
662 volume of a planktonic copepod, *Euchaeta rimana*. Mar. Biol. **140:** 871-879.
663 Fields, D. M. 2014. The sensory horizon of marine copepods, p. 157-179. *In* L. Seuront [ed.],
664 Copepods: Diversity, Habitat and Behavior. Nova Science Publishers.

Fields, D. M., D. S. Shaeffer, and M. J. Weissburg. 2002. Mechanical and neural responses from the mechanosensory hairs on the antennule of *Gaussia princeps*. Mar. Ecol. Prog. Ser. **227:** 173-186.

Fields, D. M., and J. Yen. 1993. Outer limits and inner structure: the 3-dimensional flow field of *Pleuromamma xiphias* (Calanoida: Metridinidae). B. Mar. Sci. **53:** 84-95.

---. 1997. Implications of the feeding current structure of *Euchaeta rimana*, a carnivorous pelagic copepod, on the spatial orientation of their prey. J. Plankton Res. **19:** 79-95.

Gill, C. W., and S. A. Poulet. 1986. Utilization of a computerized micro-impedance system for studying the activity of copepod appendages. J. Exp. Mar. Biol. Ecol. **101:** 193-198.

Giuffre, C., P. Hinow, H. Jiang, and J. R. Strickler. 2019. Oscillations in the near-field feeding current of a calanoid copepod are useful for particle sensing. Sci. Rep. **9:** 17742.

Gonçalves, R. J., and T. Kiørboe. 2015. Perceiving the algae: how feeding-current feeding copepods detect their nonmotile prey. Limnol. Oceanogr. **60:** 1286-1297.

Happel, J., and H. Brenner. 1983. Low Reynolds Number Hydrodynamics. Springer.

Hartline, D. K., P. H. Lenz, and C. M. Herren. 1996. Physiological and behavioral studies of escape responses in calanoid copepods. Mar. Freshw. Behav. Phy. **27:** 199-212.

Humphrey, J. A. C., R. Devarakonda, I. Iglesias, and F. G. Barth. 1993. Dynamics of arthropod filiform hairs. I. mathematical modelling of the hair and air motions. Philos. T. R. Soc. B **340:** 423–444.

Hyon, Y., Marcos, T. R. Powers, R. Stocker, and H. C. Fu. 2012. The wiggling trajectories of bacteria. J. Fluid Mech. **705:** 58–76.

Jabbarzadeh, M., and H. C. Fu. 2018. Dynamic instability in the hook-flagellum system that triggers bacterial flicks. Phys. Rev. E **97:** 012402.

688 ---. 2020. A numerical method for inextensible elastic filaments in viscous fluids. J. Comput.
689 Phys. **418:** 109643.
690 Jiang, H., C. Meneveau, and T. R. Osborn. 1999. Numerical study of the feeding current around
691 a copepod. J. Plankton Res. **21:** 1391–1421.
692 ---. 2002a. The flow field around a freely swimming copepod in steady motion. Part II:
693 numerical simulation. J. Plankton Res. **24:** 191-213.
694 Jiang, H., T. R. Osborn, and C. Meneveau. 2002b. The flow field around a freely swimming
695 copepod in steady motion. Part I: theoretical analysis. J. Plankton Res. **24:** 167-189.
696 Jiang, H., and G.-A. Paffenhöfer. 2008. Hydrodynamic signal perception by the copepod
697 *Oithona plumifera*. mar. Ecol. Prog. Ser **373:** 37-52.
698 Jiang, H., and J. R. Strickler. 2007. Copepod flow modes and modulation: a modelling study of
699 the water currents produced by an unsteadily swimming copepod. Philos. T. R. Soc. B
700 **362:** 1959-1971.
701 Jonsson, P. R., and P. Tiselius. 1990. Feeding behaviour, prey detection and capture efficiency of
702 the copepod *Acartia tonsa* feeding on planktonic ciliates. Mar. Ecol. Prog. Ser. **60:** 35-44.
703 Kallemov, B., A. P. S. Bhalla, B. E. Griffith, and A. Donev. 2016. An immersed boundary
704 method for rigid bodies. Commun. Appl. Math. Comput. Sci. **11:** 79–141.
705 Kim, S., and S. J. Karrila. 1991. Microhydrodynamics: principles and selected applications.
706 Butterworth-Heinemann.
707 Kiørboe, T., H. Jiang, R. J. Gonçalves, L. T. Nielsen, and N. Wadhwa. 2014. Flow disturbances
708 generated by feeding and swimming zooplankton. Proc. Nat. Acad. Sci. USA **111:**
709 11738-11743.

710 Kiørboe, T., and A. W. Visser. 1999. Predator and prey perception in copepods due to
711 hydromechanical signals. Mar. Ecol. Prog. Ser **179:** 81-95.
712 Kjellerup, S., and T. Kiørboe. 2012. Prey detection in a cruising copepod. Biology Lett. **8:** 438-
713 441.
714 Koehl, M. A. R., and J. R. Strickler. 1981. Copepod feeding currents: food capture at low
715 Reynolds number. Limnol. Oceanogr. **26:** 1062-1073.
716 Lim, S., A. Ferent, X. S. Wang, and C. S. Peskin. 2008. Dynamics of a closed rod with twist and
717 bend in fluid. SIAM J. Sci. Comput. **31:** 273–302.
718 Malkiel, E., J. Sheng, J. Katz, and J. R. Strickler. 2003. Digital holography of the flow field
719 generated by a feeding calanoid copepod, *Diaptomus minutus*. J. Exp. Biol. **206:** 3657-
720 3666.
721 Martindale, J. D., M. Jabbarzadeh, and H. C. Fu. 2016. Choice of computational method for
722 swimming and pumping with nonslender helical filaments at low Reynolds number. Phys.
723 Fluids **28:** 021901.
724 Olson, S. D., S. Lim, and R. Cortez. 2013. Modeling the dynamics of an elastic rod with intrinsic
725 curvature and twist using a regularized stokes formulation. J. Comput. Phys. **238:** 169–
726 187.
727 Paffenhöfer, G.-A., and K. D. Lewis. 1990. Perceptive performance and feeding behavior of
728 calanoid copepods. J. Plankton Res. **12:** 933-946.
729 Paffenhöfer, G.-A., and P. A. Loyd. 1999. Ultrastructure of setae of the maxilliped of the marine
730 planktonic copepod Temora stylifera. Mar. Ecol. Prog. Ser. **178:** 101-107.
731 Paffenhöfer, G.-A., and K. B. Van Sant. 1985. The feeding response of a marine planktonic
732 copepod to quantity and quality of particles. Mar. Ecol. Prog. Ser. **27:** 55–65.

733 Peskin, C. S. 1972. Flow patterns around heart valves: a numerical method. J. comput. phys. **10:**
734 252–271.
735 ---. 2002. The immersed boundary method. Acta Numer. **11:** 479–517.
736 Shen, X., Marcos, and H. C. Fu. 2020. How the bending mechanics of setae modulate
737 hydrodynamic sensing in copepods. Limnol. Oceanogr. **65:** 749-761.
738 Strickler, J. R. 1982. Calanoid copepods, feeding currents, and the role of gravity. Science **218:**
739 158-160.
740 Strickler, J. R., and A. K. Bal. 1973. Setae of the first antennae of the copepod Cyclops scutifer
741 (sars): their structure and importance. Proc. Nat. Acad. Sci. USA **70:** 2656-2659.
742 Svetlichny, L., P. S. Larsen, and T. Kiørboe. 2020. Kinematic and dynamic scaling of copepod
743 swimming. Fluids **5:** 68.
744 Takagi, D., and J. R. Strickler. 2020. Active hydrodynamic imaging of a rigid spherical particle.
745 Sci. Rep. **10:** 2665.
746 Tiselius, P., E. Saiz, and T. Kiørboe. 2013. Sensory capabilities and food capture of two small
747 copepods, *Paracalanus parvus* and *Pseudocalanus* sp. Limnol. Oceanogr. **58:** 1657-1666.
748 Usabiaga, F. B., B. Kallemov, B. Delmotte, A. P. S. Bhalla, B. E. Griffith, and A. Donev. 2017.
749 Hydrodynamics of suspensions of passive and active rigid particles: a rigid multiblob
750 approach. Commun. Appl. Math. Comput. Sci. **11:** 217–296.
751 van Duren, L. A., and J. J. Videler. 2003. Escape from viscosity: the kinematics and
752 hydrodynamics of copepod foraging and escape swimming. J. Exp. Biol. **206:** 269-279.
753 Vanderploeg, H. A., G.-A. Paffenhöfer, and J. R. Liebig. 1990. Concentration-variable
754 interactions between calanoid copepods and particles of different food quality:

observations and hypotheses, p. 595-613. *In* R. N. Hughes [ed.], Behavioural mechanisms of food selection. Springer.

Visser, A. W. 2001. Hydromechanical signals in the plankton. Mar. Ecol. Prog. Ser. **222:** 1-24.

Weatherby, T. M., and P. H. Lenz. 2000. Mechanoreceptors in calanoid copepods: designed for high sensitivity. Arthropod Struct. Dev. **29:** 275-288.

Weatherby, T. M., K. K. Wong, and P. H. Lenz. 1994. Fine structure of the distal sensory setae on the first antennae of *Pleuromamma xiphias* Giesbrecht (copepoda). J. Crustacean Biol. **14:** 670-685.

Yen, J., P. H. Lenz, D. V. Gassie, and D. K. Hartline. 1992. Mechanoreception in marine copepods: electrophysiological studies on the first antennae. J. Plankton Res. **14:** 495-512.

Yen, J., and N. T. Nicoll. 1990. Setal array on the first antennae of a carnivorous marine copepod, *Euchaeta norvegica*. J. Crustacean Biol. **10:** 218-224.

Yen, J., and A. Okubo. 2002. Particle and prey detection by mechanoreceptive copepods: a mathematical analysis. Hydrobiologia **480:** 165-173.

Yen, J., and J. R. Strickler. 1996. Advertisement and concealment in the plankton: what makes a copepod hydrodynamically conspicuous? Invertebr. Biol. **115:** 191-205.

Acknowledgements

Authors' contributions

X.S. and H.C.F. conceived the study and wrote the manuscript; X.S. carried out the numerical simulations and performed data analysis; X.Y. assisted in the numerical simulation. M. coordinated the study and edited the manuscript. All authors participated in discussions and gave final approval for publication.

Competing interests

We declare we have no competing interests.

Funding

This research is supported by Ministry of Education, Singapore, under its Academic Research Funds Tier 2 MOE2018-T2-2-052 and National Science Foundation award CBET-1805847.

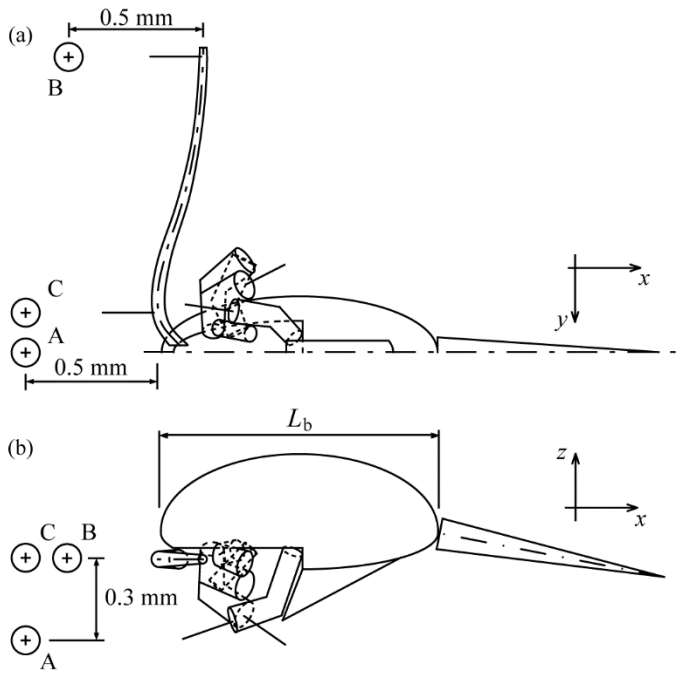

Fig. 1. (a) Ventral-dorsal and (b) lateral views of the feeding-current feeding copepod model and three starting prey positions. The cephalic appendages from left to right are the antennule, antenna, mandible, first maxilla and maxilliped. Setae (all of length 200 μm) on the proximal and distal of the antennule, the endopod of the antenna and the maxilliped, are indicated by straight lines. Prey positions B and C are centered in front of the left distal and proximal antennule setae, respectively, and A is on the sagittal plane.

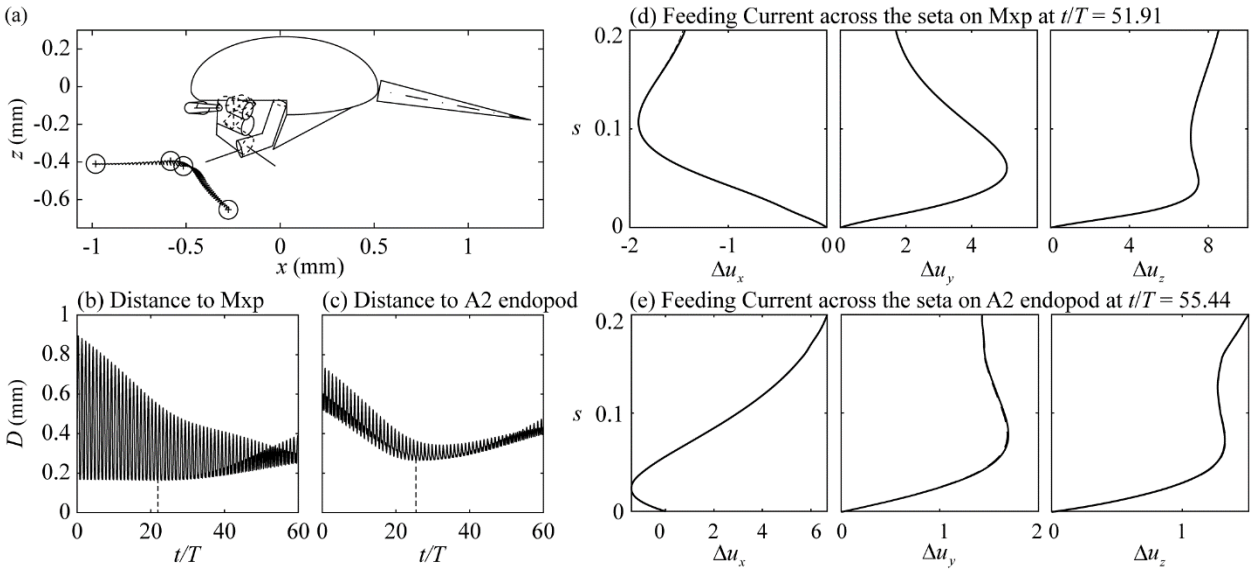

Fig. 2. (a) Side view of the prey trajectory relative to the copepod over 60 beating strokes, for a prey starting at Point A. The prey travels on the sagittal plane of the copepod. The distance from the prey center to setae on (b) the maxilliped (Mxp) and (c) the endopod of the antenna (A2) as a function of beating cycle. The instantaneous bending flow, $\Delta\mathbf{u}(s,t)$, plotted in terms of its components in the *x*, *y* and *z* direction in units of mm/s, across the setae on the (d) Mxp and (e) A2 endopod, when the distance from the prey center to the corresponding seta is the smallest. The arclength along the setal centerline (s, units of mm) is measured starting at the setal root. The solid and dashed lines represent the feeding current without and with the presence of the prey, respectively. Note that the dashed and solid lines show noticeable difference only in the middle panel in (e).

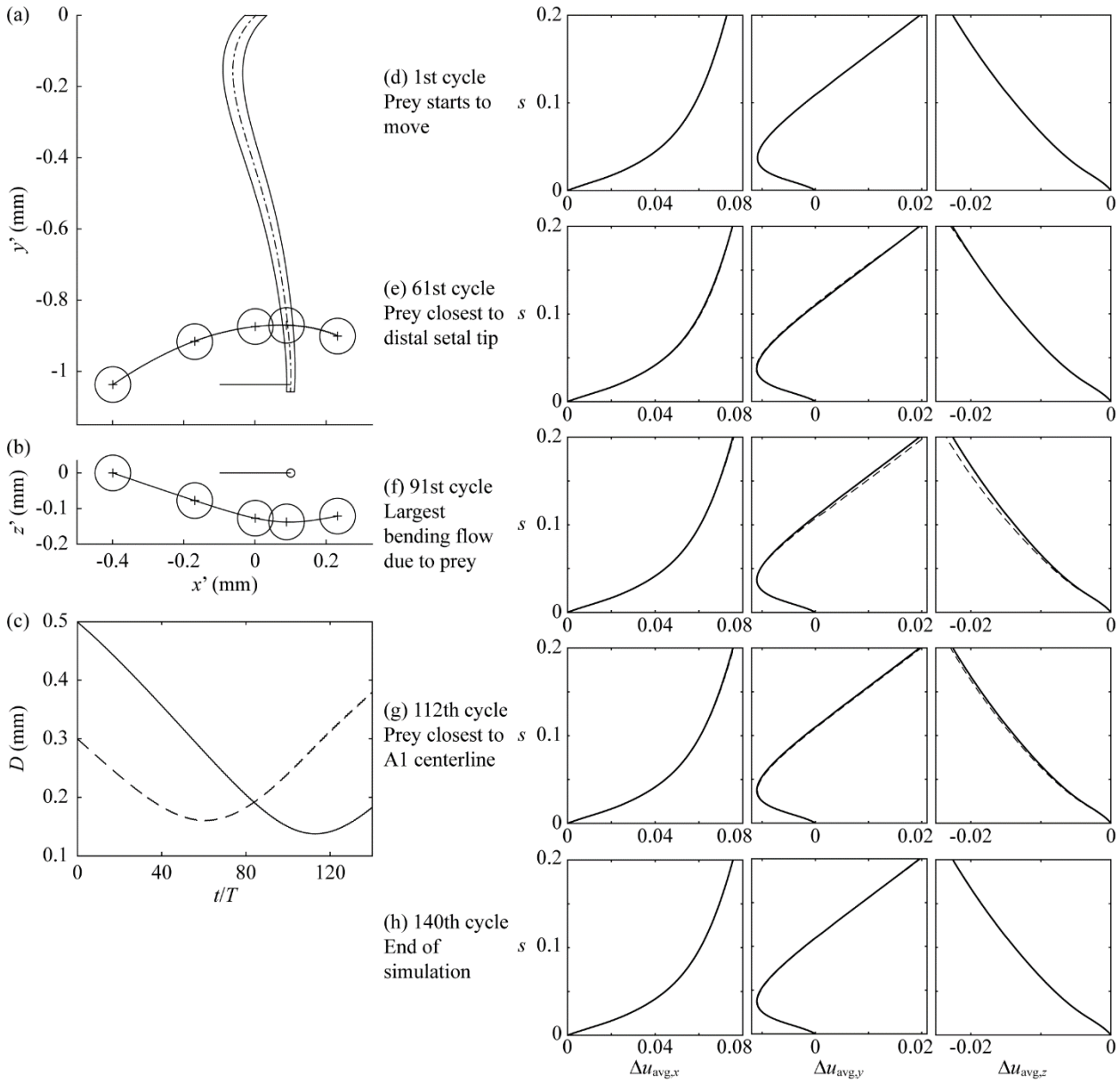

Fig. 3. (a) Ventral-dorsal and (b) side views of the prey trajectory relative to the antennule (A1) and distal seta over 140 beating strokes, for a prey starting at Point B. The large circles from left to right show the prey position at the end of the 1st, 61st, 91st, 112th and 140th beating strokes, respectively. (c) The distance from the prey center to the tip of the distal seta on A1 (dashed line) and A1 centerline (solid line) as a function of beating cycle. The time-averaged bending flow, $\Delta\mathbf{u}_{\text{avg}}(s, NT)$, plotted in terms of its components in the x, y and z direction in units of mm/s,

across the left distal seta on A1 at the (d) 1st, (e) 61st, (f) 91st, (g) 112th and (h) 140th beating stroke. The arclength along the setal centerline (s, units of mm) is measured starting at the setal root. The black solid and dashed lines represent the feeding current without and with the presence of the prey, respectively.

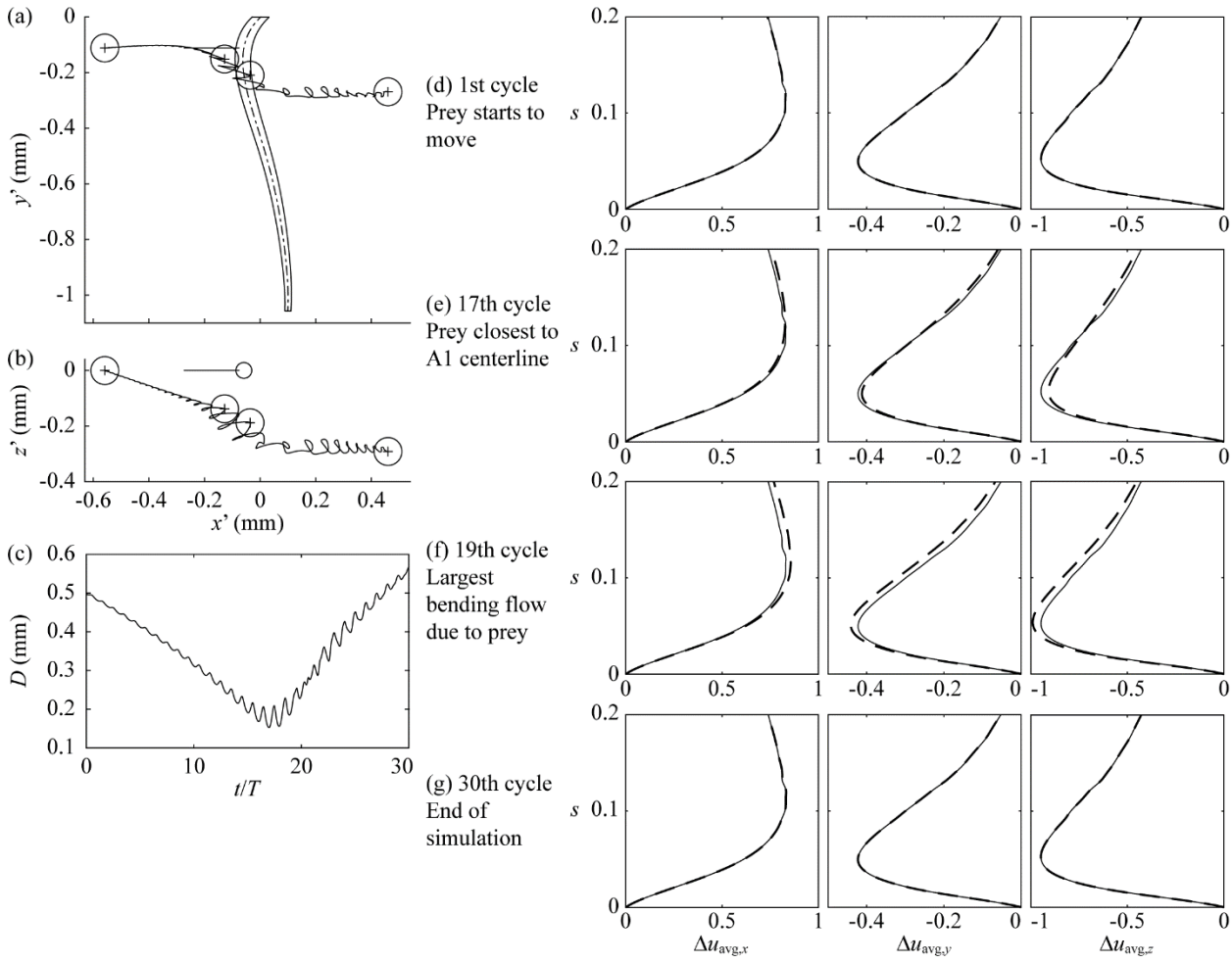

Fig. 4. (a) Ventral-dorsal and (b) side views of the prey center trajectory relative to the antennule (A1) and proximal seta over 30 beating strokes, for a prey starting at Point C. The large circles from left to right show the prey position at the end of the 1st, 17th, 19th and 30th beating strokes, respectively. (c) The distance from the prey center to the A1 centerline as a function of beating cycle. The time-averaged bending flow, $\Delta\mathbf{u}_{\text{avg}}(s, NT)$, plotted in terms of its components in the *x*, *y* and *z* direction in units of mm/s, across the proximal seta on the left A1 at the (d) 1st, (e) 17th, (f) 19th, and (g) 30th beating stroke. The arclength along the setal centerline (s, units of mm) is measured starting at the setal root. The black solid and dashed lines represent the feeding current without and with the presence of the prey, respectively.

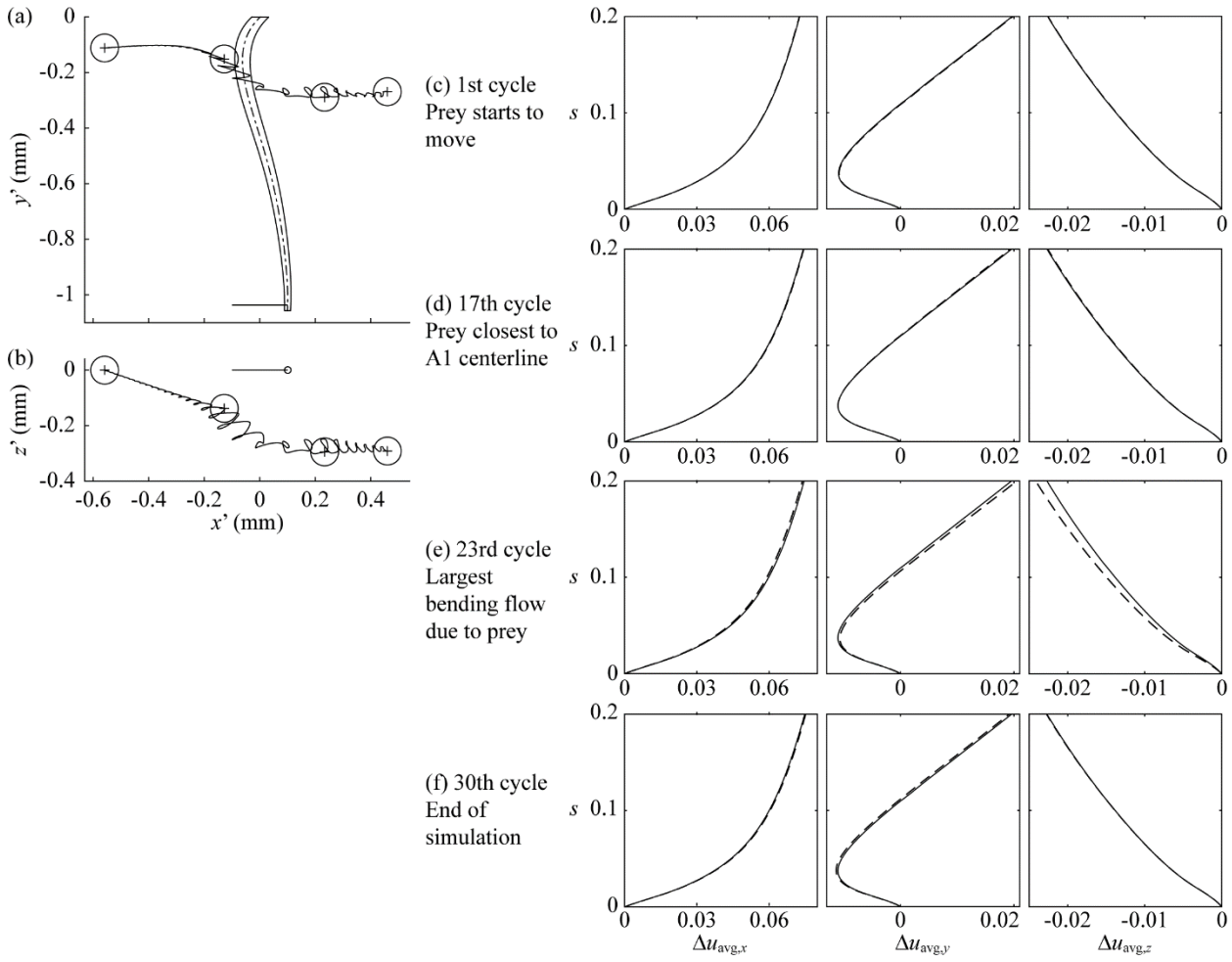

823

824 Fig. 5. (a) Ventral-dorsal and (b) side views of the prey center trajectory relative to the antennule
825 (A1) and distal seta over 30 beating strokes, for a prey starting at Point C. The large circles from
826 left to right show the prey position at the end of the 1st, 17th, 23rd and 30th beating strokes,
827 respectively. The time-averaged bending flow, $\Delta\mathbf{u}_{\text{avg}}(s, NT)$ $\Delta\mathbf{u}_{\text{avg}}(s, NT)$, plotted in terms of
828 its components in the *x*, *y* and *z* direction in units of mm/s, the across the distal seta on the left
829 A1 at the (c) 1st, (d) 17th, (e) 23rd, and (f) 30th beating stroke. The arclength along the setal
830 centerline (*s*, units of mm) is measured starting at the setal root. The solid and dashed lines
831 represent the feeding current without and with the presence of the free-floating prey, respectively.

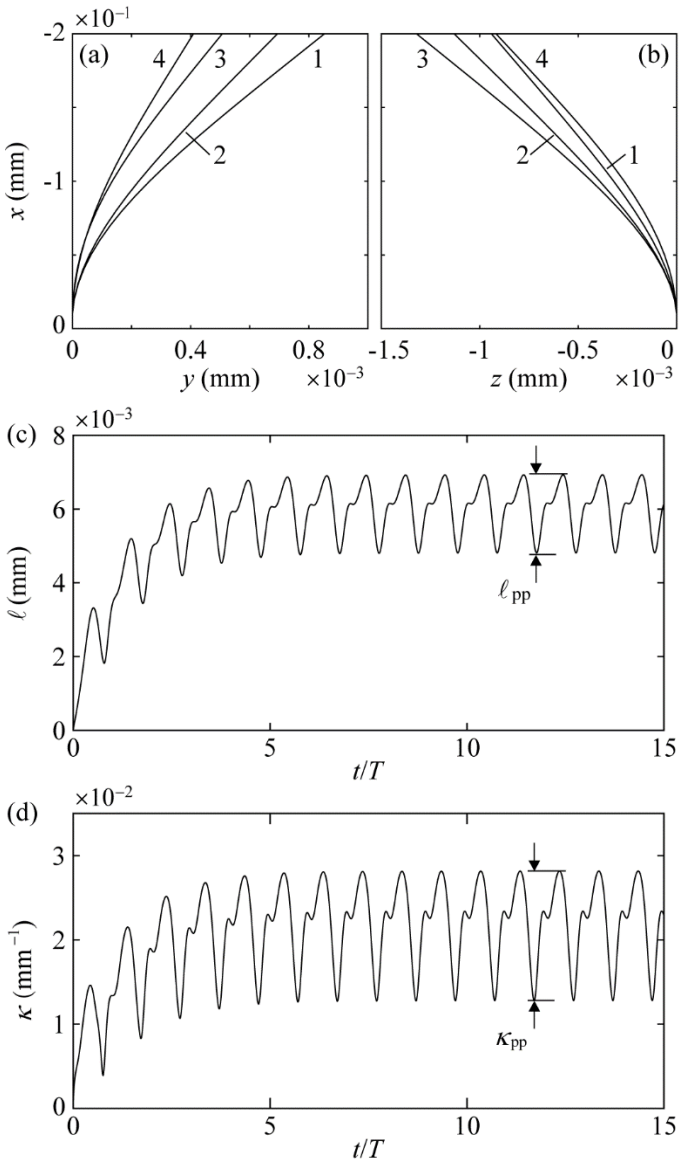

Fig. 6. (a,b) Projected views of the shape of the distal seta without the presence of the prey, after the time-averaged bending flow, $\Delta\mathbf{u}_{\text{avg}}(s,t)$, across the distal seta reaches the steady state. A sequence of shapes at equally spaced times during one cycle of the beating stroke are labeled by the numbers 1-4. Plots of the magnitudes of (c) the tip displacement ℓ and (d) root curvature κ of the distal seta as a function of time t without the presence of the prey. The peak-to-peak amplitudes of the tip displacement and root curvature are defined as ℓ_{pp} and κ_{pp}, respectively.

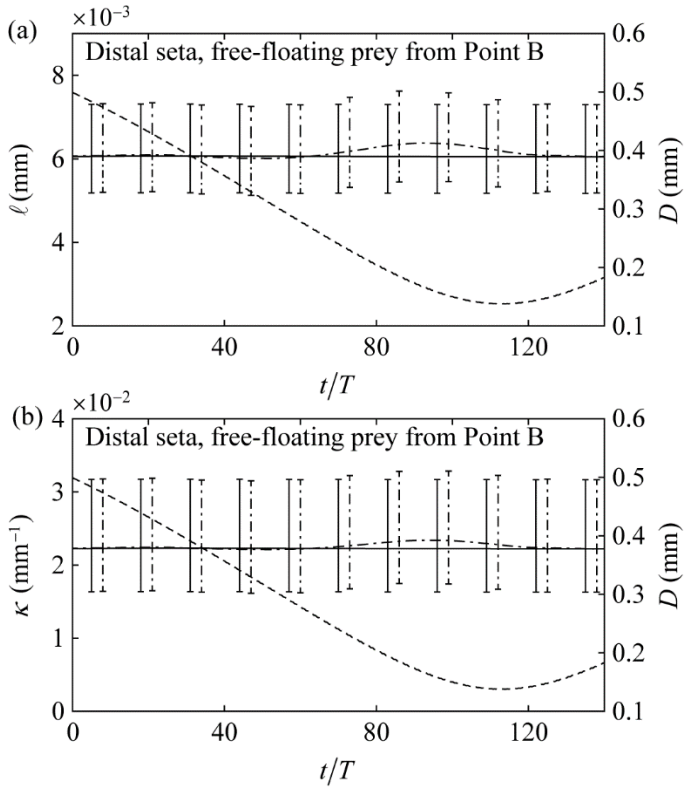

839

840 Fig. 7. Plots of the (a) magnitude of tip displacement, ℓ, and (b) magnitude of root curvature, κ,
841 of the distal seta on the antennule (A1) as a function of beating cycle, for a free-floating prey
842 starting at Point B and moving along the trajectory shown in Figs. 3a,b. The solid lines in all
843 panels represent the setal response without the presence of the prey, while the dash-dotted lines
844 represent the setal response due to the entrained prey. The dashed lines in all panels denote the
845 distance from the prey to the A1 centerline, *D*. The vertical bars represent the peak-to-peak
846 amplitudes of the setal (a) tip displacement and (b) root curvature.

847

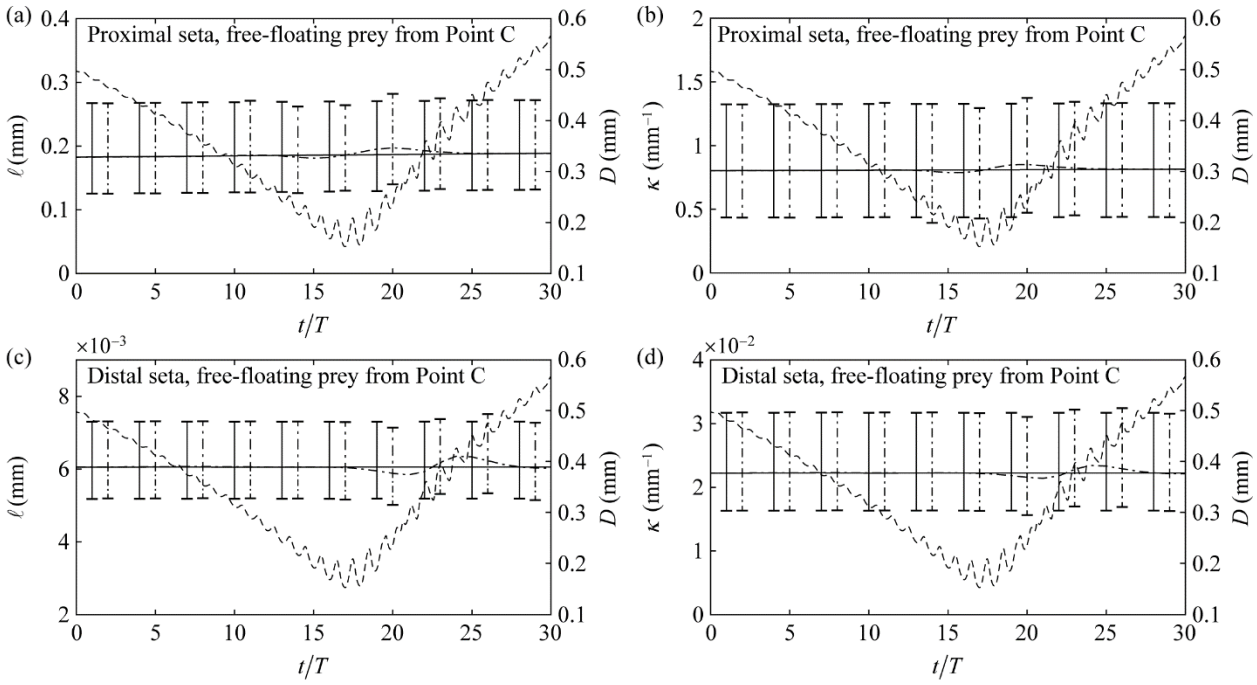

Fig. 8. Plots of the (a,c) magnitude of setal tip displacement, ℓ, and (b,d) magnitude of root curvature, κ, of the two setae on the antennule as function of beating cycle, for a free-floating prey starting at Point C and moving along the trajectory shown in Figs. 4a,b and 5a,b. The solid lines in all panels represent the setal response without the presence of the prey, while the dash-dotted lines represent the setal response due to the entrained prey. The dashed lines in all panels denote the distance from the prey to the centerline of the antennule, D. The vertical bars represent the peak-to-peak amplitudes of the setal (a,c) tip displacement and (b,d) root curvature.